AIAA JOURNAL
Vol. 41, No. 3, March 2003

High-Resolution Large-Eddy Simulation of Flow Around Low-Pressure Turbine Blade

B. Raverdy,* I. Mary,† and P. Sagaut†
ONERA, 92322 Châtillon Cedex, France
and
N. Liamis‡
SNECMA Moteurs, 77550 Moissy-Cramayel, France

Large-eddy simulation of compressible Navier–Stokes equations is used to study flows where a laminar boundary-layer separation is followed by a turbulent reattachment. The aim of the present work is to predict and describe the transition process and its interaction with the wake dynamics for a subsonic blade turbine configuration. Indeed, a better knowledge of this mechanism can help to improve the accuracy of a Reynolds-averaged Navier–Stokes turbulence model for such a flow case. High-resolution large-eddy-simulation-type computations have been carried out for the T106 low-pressure blade turbine at inlet Mach number of 0.1 and chord Reynolds number of 1.6×10^5 based on the exit isentropic velocity. The simulated mean and turbulent quantities compare well with the available experimental data. The primary two-dimensional instability that originates from the free shear in the bubble is unstable via the Kelvin–Helmholtz mechanism. Then, the three-dimensional motions spread on the boundary layer, leading to full breakdown to turbulence after the reattachment point.

Nomenclature

C	=	axial blade chord
$\bar{F}_j$	=	filtered Euler fluxes
$\bar{F}_j^v$	=	filtered viscous fluxes
g	=	pitch
L_z	=	spanwise extend of the computational domain
l_b	=	length of the separation bubble
$\langle l_b \rangle$	=	average length of the separation bubble
M_0	=	Mach number
N_k	=	number of cells in the spanwise direction
Pr	=	Prandtl number
$\bar{Q}$	=	filtered conservative flow variables
Re	=	Reynolds number
$\bar{u}_j$	=	filtered velocity component
x_r	=	location of the reattachment
x_s	=	location of the separation
γ	=	specific heat ratio
δ_{ij}	=	Kronecker tensor
ϕ_{rms}	=	root-mean-square quantity

Subscripts

0	=	reference quantity
∞	=	upstream condition

Introduction

In many engineering flows around wings and blades, transition and separation phenomena are strongly coupled through a laminar separation bubble.[1] Depending on the geometry and the Reynolds number,[2] the boundary layer often separates while still laminar; the detached shear layer might become turbulent rapidly enough to reattach, leading to the formation of a "short" bubble. Although the size of the bubble is generally small compared to the chord of the body, this recirculation zone has sometime a major impact on the global dynamics of the flow. For instance, this bubble is often of particular importance for the design of high-lift devices on aircraft or those of gas turbines. In the past, Reynolds-averaged Navier–Stokes (RANS) modeling approaches have been used to predict this kind of flow (for instance, see Ref. 3). However the transitional behavior of the boundary layer and the high unsteadiness of the separation process tend to limit the predictive capability of RANS simulations. Indeed this approach still suffers from its lack of accuracy when transition or separation phenomena drive the global dynamics of the flow. Therefore this transition process has motivated a large amount of work because a better knowledge of the flow dynamic can help to improve the accuracy of RANS turbulence models. For this purpose large-eddy simulation (LES) and direct numerical simulation (DNS) are viewed more and more frequently as complementary tools to wind-tunnel experiments. Indeed, the increase of the computational capability allows nowadays the handling of LES of flows with Reynolds numbers up to 10^6 on a simple geometry.[4] Furthermore, DNS and LES have the advantage for transitional flow to be free of some experimental unreliabilities like side-wall effects, freestream disturbances, or the surface roughness. Recently, DNS of a transitional separation bubble on a flat surface caused by aspiration through an opposite boundary were realized by different researchers.[5–9] LES was used in Ref. 10 to study the separation bubble induced by a change of curvature. In this case the geometry was a simple flat plate with a semicircular leading edge. If these results are useful to better understand the transition process occurring in some external flows, their interest for the study of internal flows seems less attractive. Indeed the flat plate and the freestream condition employed in these works do not allow the representation of blockage and curvature effects, as well as the unsteady wake of the blade. Now these parameters can have a deep impact on the transition phenomenon occurring in a gas turbine. Therefore the aim of this paper is to gain deep insight into the flow dynamics associated with some specific blade profiles of a low-pressure turbine (LPT) and to provide a reliable database for future developments dealing with transition models for RANS simulation. Different experimental works[11–13] have been carried out to characterize the transition process in LPT during the last decade, which appears quite influenced by the level of freestream disturbances. The DNS realized by Wu and Durbin[14] was focused on the study of bypass transition caused by the influence of a periodic upstream wake, which generates a high level of freestream disturbances. In

Received 25 March 2002; revision received 5 October 2002; accepted for publication 5 October 2002.

*Ph.D. Student, 29 avenue de la Division Leclerc.
†Scientist Engineer, 29 avenue de la Division Leclerc.
‡Aero and Cooling Turbine Research and Methods Manager, Centre de Villaroche.

the present paper the emphasis is put on the transition process without upstream wake. As the mesh resolution is a crucial numerical parameter for the accuracy of the simulation, several meshes have been used to check the grid convergence of the solution. Despite the low value of the Reynolds number in the LPT [$\mathcal{O}(10^5)$], the computational cost of the simulation is quite expensive. Therefore a local mesh refinement technique is used to reduced the computational cost. Once the simulation validated thanks to a comparison with Hodson's experiment,[13] the transition process was analyzed with the stress put on the unsteady character of the laminar separation bubble.

The paper is organized as follows. The governing equations are presented in the next section, and the numerical method is described in the third section. The fourth section is devoted to the presentation of the test case, the LES validation, and the transition mechanism analysis.

Mathematical Model

Filtered Navier–Stokes Equations

A dimensionless form of the three-dimensional unsteady filtered Navier–Stokes equations is used for a viscous compressible Newtonian fluid. Any flow variable ϕ can be written as $\phi = \bar{\phi} + \phi'$, where $\bar{\phi}$ represents the large-scale part of the variable and ϕ' its small-scale part. The filtering operator, classically defined as a convolution product on the computational domain, is assumed to commute with time and spatial derivatives. Moreover it is convenient for the clarity of the equations to introduce the Favre filtering, $\tilde{\phi} = \overline{\rho\phi}/\bar{\rho}$. In conservative form the filtered Navier–Stokes equations can be expressed in three-dimensional Cartesian coordinates (x_1, x_2, x_3) as

$$\frac{\partial \bar{Q}}{\partial t} + \frac{\partial \bar{F}_j}{\partial x_j} - \frac{1}{Re}\frac{\partial \bar{F}_j^v}{\partial x_j} = 0 \tag{1}$$

The Reynolds number is defined as $Re = \rho_0 u_0 L_0/\mu_0$. The symbols u_0, ρ_0, L_0, and μ_0 denote a characteristic velocity, density, length, and dynamic viscosity, respectively. The conservative flow variables are defined as $\bar{Q} = [\bar{\rho}, \bar{\rho}\tilde{u}_1, \bar{\rho}\tilde{u}_2, \bar{\rho}\tilde{u}_3, \bar{p}/(\gamma-1) + \bar{\rho}\tilde{u}_j\tilde{u}_j/2]^T$ and the inviscid fluxes by $\bar{F}_j = \tilde{u}_j\bar{Q} + (0, \delta_{1j}\bar{p}, \delta_{2j}\bar{p}, \delta_{3j}\bar{p}, \bar{p}\tilde{u}_j)^T$. By using Boussinesq eddy viscosity hypothesis, the viscous fluxes are given by $\bar{F}_j^v = (0, \bar{\sigma}_{1j}, \bar{\sigma}_{2j}, \bar{\sigma}_{3j}, \bar{\sigma}_{kj}\tilde{u}_k + \hat{q}_j)^T$, with

$$\hat{\sigma}_{ij} = [\mu(\tilde{T}) + \mu_t]\left(\frac{\partial \tilde{u}_i}{\partial x_j} + \frac{\partial \tilde{u}_j}{\partial x_i} - \frac{2}{3}\delta_{ij}\frac{\partial \tilde{u}_k}{\partial x_k}\right) \tag{2}$$

$$\hat{q}_j = \frac{[\mu(\tilde{T}) + \mu_t]}{Pr}\frac{\partial \tilde{T}}{\partial x_j} \tag{3}$$

where the eddy viscosity μ_t must be expressed by a subgrid-scale model (for more details, see Ref. 15). These equations are supplemented with the filtered equation of state, thanks to the reference Mach number M_0:

$$\bar{p} = (\bar{\rho}\tilde{T})\Big/\left(\gamma M_0^2\right) \tag{4}$$

Subgrid-Scale Modeling

This work has been carried out with the monotonic integrated large-eddy simulation (MILES) approach,[16] which does not explicitly use a subgrid-scale model based on physical assumptions. As a consequence, the eddy viscosity in Eqs. (2) and (3) is set to zero. Thus the intrinsic dissipation of the numerical scheme is assumed to transfer the energy from the large scales to the small ones. This technique must be used with some cautions because the result can be influenced by the choice of both the dissipative scheme used to discretize the Euler fluxes and the mesh resolution. However, it has been shown that this approach can give satisfactory results for complex applications,[17,18] as long as sufficient small turbulent eddies are present in the simulation. This requires the use of an adapted scheme and a grid resolution slightly finer than those usually employed in classical LES (with explicit subgrid-scale modeling and central differencing).[19,20]

Numerical Method

General Description

The solver FLU3M,[21] developed by ONERA, is based on a cell-centered finite volume technique and structured multiblock meshes. The viscous fluxes are discretized by a second-order-accurate centered scheme. For efficiency purpose an implicit time integration is employed to deal with the very small grid size encountered near the wall. Then a three-level backward differentiation formula is used to approximate the temporal derivative of Q in Eq. (1), leading to second-order accuracy. An approximate Newton method is employed to solve the nonlinear problem. At each iteration of this inner process, the inversion of the linear system relies on the lower-upper symmetric Gauss–Seidel implicit method. More details about these numerical points are available in Ref. 21. The Euler fluxes are discretized by a modified AUSM + (P) upwind scheme, which is fully described in Ref. 4. The numerical dissipation of the scheme is assumed to transfer the energy from the large scales to the small scales at a rate nearly equivalent to the one provided by a usual subgrid-viscosity model. This numerical method is the same as the one developed to perform LES of the flow around a two-dimensional wing profile in near-stall conditions[4] and also successfully used to compute LES of the flow over a cavity at high Reynolds number.[18]

Local Mesh Refinement Technique

LES of complex flows at a realistic Reynolds number requires a huge amount of grid points. Therefore it becomes crucial to optimize the cell distribution in order to limit the total number of grid points. For the flow case considered in this study, the flow remains laminar and two-dimensional in a large zone of the computational domain. Indeed the blade is supposed to be of infinite span, whereas the flow is laminar and uniform at the inflow. Therefore, the boundary layer often remains laminar in a large part of the pressure and suction sides of the blade. Thus three-dimensional computation can be limited to turbulent regions of the boundary layer and to the wake. Such as a method is employed in Ref. 4 to compute the flow around an airfoil through a two-/three-dimensional coupling technique. However a more improved method is employed in this study to allow the use of three-dimensional domain with different spanwise resolution, as illustrated by the Fig. 1. Indeed the spanwise size of the turbulent structure is larger in the far wake than near the trailing edge.[22] Thus coarser spanwise resolution are used in the far wake to decrease the computational cost. As the domain interface Γ between coarse and fine grid resolution is located in a turbulent zone, the discontinuity in the characteristic lengths involves a discontinuity in the spectral representation of the flowfield.[23] Therefore a frequential restriction procedure is needed to transfer informations from the fine mesh resolution to the coarse one, whereas a frequential enrichment procedure is used for the inverse way. Numerically, this coupling is achieved through the use of ghost cells at the interface. The information transfer between the solutions on the fine and coarse grid (noted Q_f and Q_c, respectively) is realized by applying a low-pass filter to Q_f. This low-pass filter, based on a simple average in the spanwise direction, leads to the following definition of Q_c^{ghost}:

$$Q_c^{\text{ghost}} = \frac{N_k^c}{L_z}\int_0^{L_z/N_k^c} Q_f \, dz \tag{5}$$

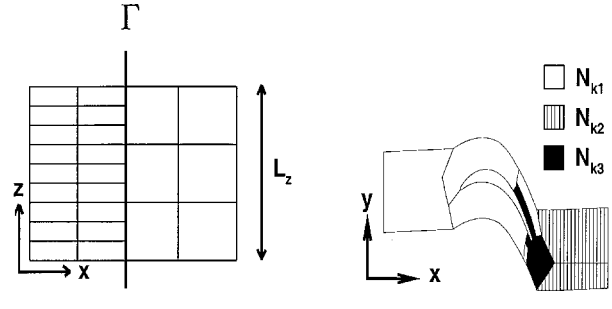

Fig. 1 Grid decomposition into different spanwise mesh resolution.

where N_k^c denotes the number of cells of the coarse domain in the spanwise direction. This length is the same for all subdomains. Finally a first-order extrapolation is used to regenerate from Q_f the high frequencies information required by the enrichment procedure, leading to the following definition of Q_f^{ghost}:

$$Q_f^{\text{ghost}} = Q_c + \left(Q_f - Q_c^{\text{ghost}}\right) \tag{6}$$

As this procedure is slightly less accurate than those developed by Quéméré et al.,[23] the interface located in a turbulent zone should be placed sufficiently far from the blade to prevent a spurious interaction between this boundary condition and the transitional flow.

Numerical Results

T106 Test Case

The T106 low-pressure turbine blade has been retained for this work. Measurements of velocity and Reynolds-stress profiles have been carried out by Hodson[13] for a wide range of Reynolds numbers and different level of inflow disturbances. The present study focuses on the simulation of the case with laminar inflow. The Reynolds number is set equal to 1.1×10^5 based on the inlet velocity u_∞ and the axial blade chord C. The inlet Mach number is equal to 0.1, with inlet and exit angle equal to 37.7 and -63.2 deg, respectively. The normalized pitch g/C, which represents the distance between two blades profile in plane grid representation, is equal to 0.93. With these flow parameters the boundary layer on the pressure side remains laminar, whereas transition occurs between $x/C = 0.8$ and 0.9 on the suction side thanks to a laminar separation bubble.

Computational Setup

In the (x, y) plan the grid topology is illustrated in Fig. 2 (one out of four grid point is shown). The decomposition is based on two H-grids (upstream and downstream sections) and one O-grid around the blade. Indeed the slope discontinuities associated with the use of an H-grid around the blade tend to generate some spurious oscillations at the leading and trailing edge, even if a DNS is used.[14] The computational domain ranges from $x/C = -1$ (inflow plan) to $x/C = 2$ (outflow plan). To check the results' sensitivity to some grid parameters, several meshes have been defined, whose characteristics are given in Table 1. In the (x, y) plane the three different grids employed for this study are all identical. These grids are denoted by $g1$, $g2$, or $g3$ in the following part of the paper. A fine LES mesh resolution must be used to obtain reliable results because the MILES approach is employed for the subgrid-scale modeling. In the streamwise direction the resolution is always less than 18 wall units in the turbulent boundary layer. In the transitional zone this value ranges from five to eight as a result of the decrease of the skin-friction coefficient associated with the separation bubble. In fact around 250 points are located between the starting point of the transition process and the trailing edge. In the wall normal direction around 50 points are located in the boundary-layer thickness δ_{99} at the transition point and the trailing edge. The size of the first cell corresponds to $\Delta y^+ < 1$, and a smooth stretching of 5% is used. It has been demonstrated in Ref. 24 that such resolution in the (x, y) plane is appropriate. As the flow remains laminar in the pressure side,[12] only two-dimensional block are used from $x/C = 0.94$ (on the pressure side) to $x/C = 0.77$ (on the suction side) to limit the number of points. In the turbulent part of the suction side boundary layer, the three-dimensional block extends to $0.1C$ in the wall normal direction. This length is clearly sufficient to avoid the possible spanwise filtering of the turbulent structures related to the local mesh refinement technique because it is approximately three times larger than the boundary-layer thickness at the trailing edge. The gk grids ($k = 1, 3$) only differ by their spanwise characteristics. On the one hand, the $g1$ and $g2$ meshes highlight the effect of the spanwise resolution, characterized by a Δz^+ less than 10 and 20, respectively. These two grids have the same spanwise extent $L_z/C = 0.032$, which corresponds approximately to the boundary-layer thickness at the trailing edge. On the other hand, the $g1$ and $g3$ meshes, with spanwise extent of $0.032C$ and $0.064C$ respectively, allow us to check the influence of this parameter because their spanwise resolution are equal.

Table 1 Grid description

	Grid		
Parameter	$g1$	$g2$	$g3$
N_i	920	920	920
N_j	80	80	80
N_{k1}, N_{k2}, N_{k3}	2/10/30	1/5/15	4/20/60
Δx^+ (DNS : $\Delta x^+ < 20$)	<18	<18	<18
Δy^+ (DNS : $\Delta y^+ < 2$)	<1	<1	<1
Δz^+ (DNS : $\Delta z^+ < 7$)	<10	<20	<10
Spanwise distance L_z	3.2%	3.2%	6.4%
Number of points	10^6	5.10^5	2.10^6

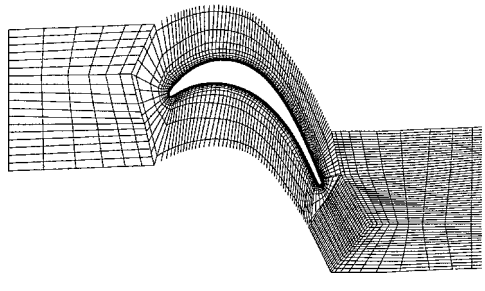

Fig. 2 Computational grid (one out of four grid points is shown).

All of the simulations are carried out with a time step equal to $1.07 \times 10^{-4} C/u_\infty$. The maximum Courant–Friedrichs–Lewy numbers based on the acoustic and entropic/vortical wave speeds are less than 11 and 1, respectively. Around five time units are necessary to get a well-established unsteady solution from a steady RANS initial solution. For the average quantities the averaging procedure is performed in the homogeneous spanwise direction and in time over a period of 6 C/u_∞. The simulations are carried out on a single processor of NEC SX5, and the code is running approximately at 4G-flops (for a crest speed of 8G-flops). Almost 240 CPU hours are needed to performed the time integration over a period of 6 C/u_∞ on the largest grid $g3$.

Validation

To validate the present simulations, both mean flow and rms quantities are compared with experimental data of Engber and Fottner[12] for the pressure coefficient and Hodson[13] for the velocity field. A comparison of pressure coefficient is displayed in Fig. 3a, where the results of the DNS (57×10^6 grid points) of Wu and Durbin[14] performed with the same geometry and inflow condition are also plotted. The results are in satisfying agreement with available experimental data. Indeed different reasons can explain the small discrepancies between Engber and Fottner experiment and the simulation: in the experiment the Reynolds and Mach numbers are around three time larger, whereas the freestream turbulence level is between 1 and 4%. As the laminar separation bubble is quite sensitive to these parameters, it is not surprising that small discrepancies occur between experimental data and simulations. Furthermore the results are nearly identical to those of the DNS carried out in Ref. 14. The pressure plateau around $x/c = 0.9$ and the sudden deacrese of Cp downstream of this position underlines the presence of a laminar separation bubble followed by a turbulent reattachment (for instance, see Refs. 4, 8, and 9). Figure 3b presents a comparison of the mean velocity magnitude profiles computed on the different grids with those of Hodson's experimental data. Grid resolution and spanwise extent are not seen to have a significant effect in the present computations, showing that a grid convergence is reached. The results are in very good agreement with the experiments. Figure 3c, which represents the mean skin-friction coefficient on the suction side, confirms the presence of a separated zone. As the experimental skin-friction coefficient is not available, the experimental velocity profiles are used to roughly estimate this quantity. Then, the results are in good agreement with experimental data because a separation bubble is also detected in the experiment. The laminar separation occurs around $x_s/C = 0.83$, whereas the turbulent reattachment is located around $x_r/C = 0.95$. The length of the bubble is denoted by l_b in the following part of the paper. After the reattachment the sudden increase of the skin-friction coefficient is explained by the

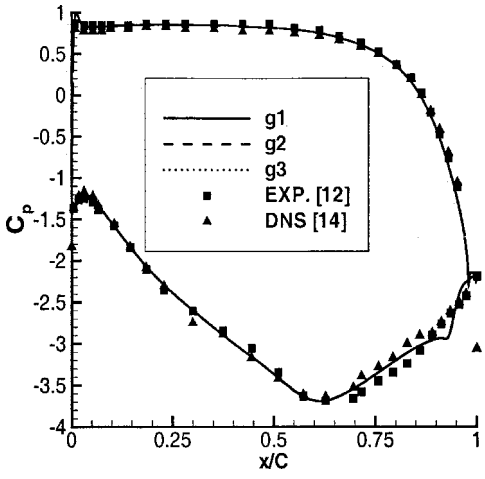

a) Mean pressure coefficient

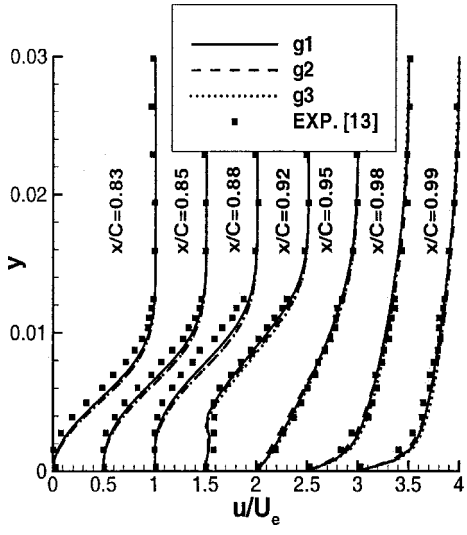

b) Mean velocity profiles

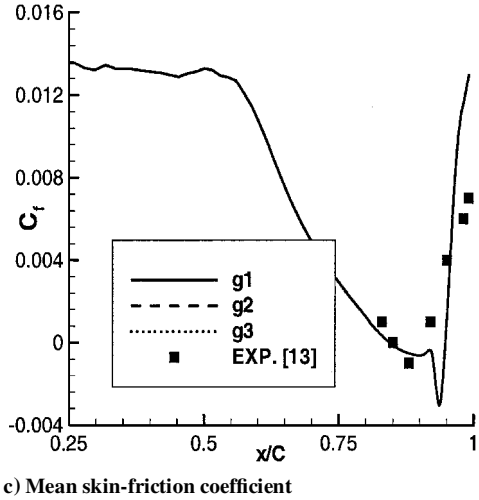

c) Mean skin-friction coefficient

Fig. 3 Influence of spanwise resolution and extent.

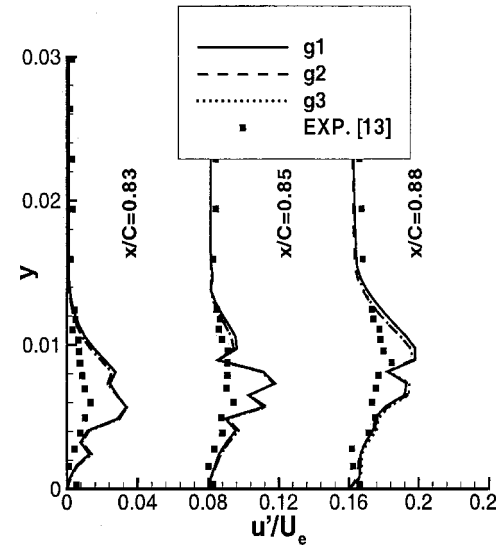

a)

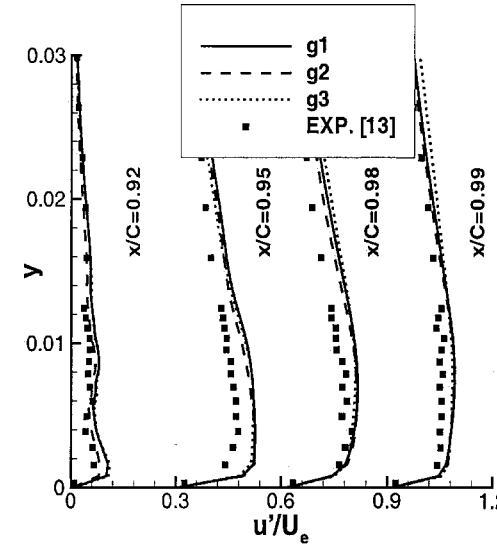

b)

Fig. 4 Influence of spanwise resolution and extent on rms velocity profiles a) in the laminar bubble and b) downstream of the laminar bubble.

fact that the boundary layer becomes fully turbulent. The rms velocity profiles are represented on Fig. 4 from $x/C = 0.83$, where the flow is separated and laminar, to $x/C = 0.99$, where it is fully turbulent. The transition is observed to occur slightly upstream of the reattachment point around $x/C = 0.92$. This location is determined as the point where the spanwise velocity fluctuation becomes larger than 1% of the external boundary-layer velocity. Downstream of the mean reattachment point, the maximum rms value rapidly increases to reach a level close to 15% of the external velocity, corresponding to a fully developed turbulent flow. Differences observed upstream of $x/C = 0.92$ between the different computations and the experimental data are thought to be meaningless because they correspond to very low values that might be very sensitive to wind-tunnel operating conditions. Another interesting conclusion is that a realistic description of the flow is obtained, even with relative thin domains in the spanwise direction, showing that there is a decorrelation between large scales of the flow and the smallest ones, which are responsible for the transition process. The same conclusion was drawn from LES calculations of the flow around an airfoil presented in Ref. 4.

Analysis of Transition to Turbulence

The preceding validations show that the LES results are reliable, that is, realistic physical phenomena are present and an analysis can be carried out from the simulations.

The onset of transition takes place in the separation bubble on the suction side, and underlying physical mechanisms can be very dependent on the structure of the bubble and external forcing. The definition of separation and reattachment used in the precedent paragraph is related to positions where the mean skin friction vanishes. More accurate descriptions of separation/detachment can be obtained considering the fraction of time γ that the flow is reversed very near the wall (see Fig. 5). Following Simpson,[25] incipient detachment (ID) (respectively, reattachment, IR) occurs with reverse flow 1% of the time, intermittent transitory detachment (ITD, respectively, ITR) occurs with instantaneous backflow 20% of the time,

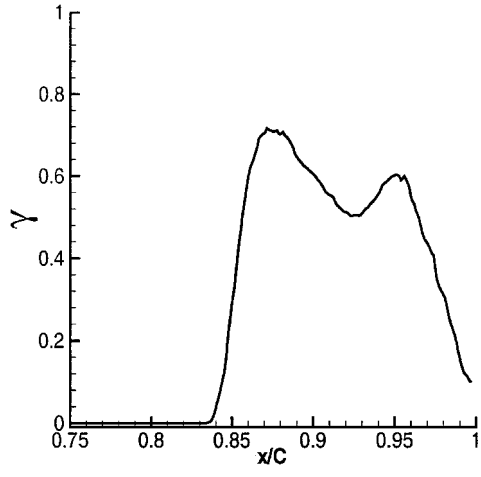

Fig. 5 Fraction of time of reverse flow along the suction side.

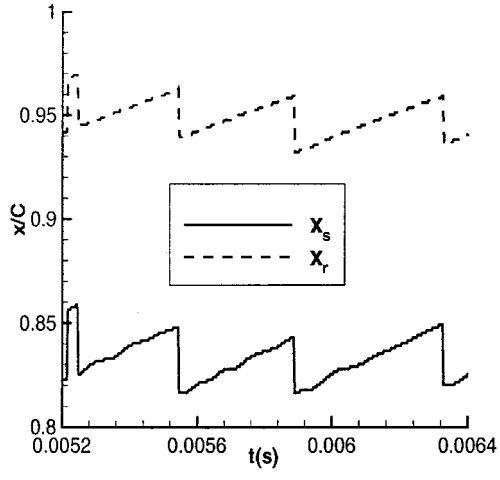

Fig. 6 Separation and reattachment locations at midspan in function of the time.

transitory detachment (TD, respectively, TR) occurs with instantaneous backflow 50% of the time, and detachment (D, respectively, R) occurs where the time-averaged skin friction is zero. Looking at Fig. 5 reveals that in the present case ITR is missing because of the neighborhood of the trailing edge. So, a strong influence of the flow in the trailing-edge region on the bubble can be expected. The wavy distribution of γ inside the bubble has already been observed in other simulations.[8,26]

The distribution of γ shows that the instantaneous separation and reattachment points are moving along the suction side. Histories of instantaneous separation and reattachment positions are displayed in Fig. 6. It is seen that they both are subjected to large spatial variations, but a very interesting fact is they are locked in phase, resulting in a nearly constant bubble length.

To get a better description of the bubble, the maximum intensity of the backflow associated with the Reynolds-averaged velocity field as a function of the position along the suction side is plotted in Fig. 7. It is seen that the maximum reverse flow is close to 6% of the external velocity U_e. This value is similar to those found in the DNS of Alam and Sandham[8] (4 to 8%) or the LES of Yang and Voke[10] (3%) for short bubbles. Spalart and Strelets[9] observed higher values (23%) on a 10 times longer bubble. In the present configuration the mean value of the bubble length $\langle l_b \rangle$ is equal to 10 δ^s_{99} or, equivalently, 120 δ^s_θ, where δ^s_{99} and δ^s_θ are the boundary-layer thickness and the momentum thickness at the separation point, respectively, which is an intermediary value between the cases considered by Alam and Sandham ($\langle l_b \rangle / \delta^s_\theta \approx 40$) and those of Spalart and Strelets[9] ($\langle l_b \rangle / \delta^s_\theta \approx 400$). Linear stability analysis shows that backflows as high as 15–20% of U_e are required to obtain absolutely instable profiles. As a consequence, a global feedback must exist in the present configuration to obtain self-sustained fluctuations in the bubble. This mechanism is analyzed in the next section.

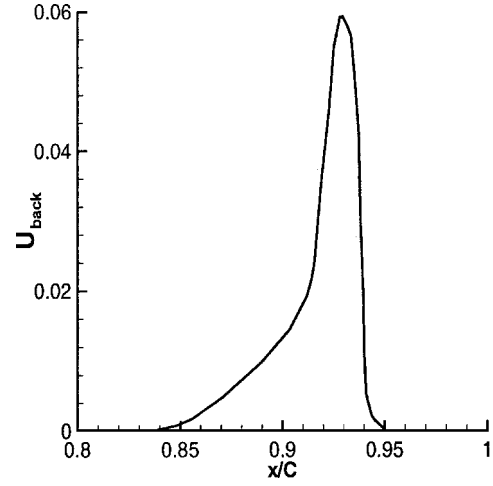

Fig. 7 Backflow intensity in the suction side boundary layer ($U_{\text{back}} = |\min(u)|/u_e$).

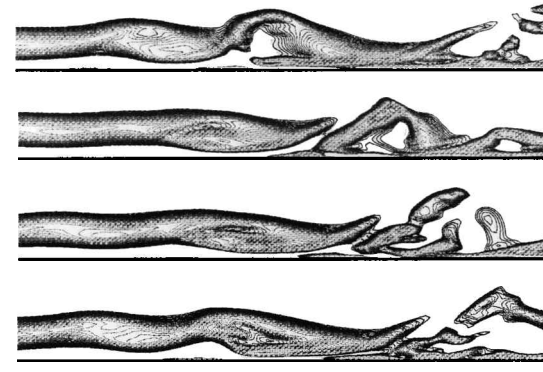

Fig. 8 Instantaneous spanwise vorticity in the (x, y) plane near the bubble.

A view of the instantaneous flow in the bubble region at different times is given in Fig. 8. The roll up of the separated shear layer and the ejection of coherent structures are clearly identified, in agreement with observations done during previous numerical studies.[8–10] Many authors have tied this roll-up to the Kelvin–Helmholtz (KH) instability. To evaluate the characteristic scales of the fluctuations in the present case, the wave-number/frequency spectrum of the pressure fluctuations at the wall at a position located inside the bubble is shown in Fig. 9b. It is seen that two types of fluctuations are present: acoustic fluctuations moving upstream at the speed $|U_e - c| = 270\ \text{m} \cdot \text{s}^{-1}$ and vortical disturbances convected downstream at speed $U_c = 36\ \text{m} \cdot \text{s}^{-1} \approx 0.6 U_e$. The latter correspond to the convection of the structures observed in Fig. 8. The value of U_c is in agreement with the classical value observed in separated shear layer and is close to predictions given by the linear stability theory of the KH modes. The spatial period λ of these structures is computed as the distance between two vortices with the same sign of spanwise vorticity component (see Fig. 10). A global estimation yields $\lambda = 0.054C$. The associated frequency is then $f_c = 3500$ Hz. The corresponding Strouhal number, based on U_e and $\langle l_b \rangle$, is equal to 0.24. As underlined by Yang and Voke,[10] another criterion has to be satisfied in order to get the KH instability: $0 < kh < 1.2785$, where k is the wave number deduced from λ and h is the shear-layer thickness. In the present computation we get $kh = 1.16$, which allows the growth of the KH modes. Spalart and Strelets[9] remarked that this mechanism can lead to a very fast growth of the initial perturbations, resulting in the appearance of two-dimensional vortices within one spatial period. (This can be seen in Fig. 8.)

To get a deeper understanding of the way the upstream disturbances are amplified inside the recirculation bubble, the streamwise velocity rms fluctuation profiles at three positions are displayed in Fig. 11. At the first position ($x/C = 0.83$), very close to the separation point, the profile exhibits one peak located at the center of the boundary layer. At the second position ($x/C = 0.88$) at the center

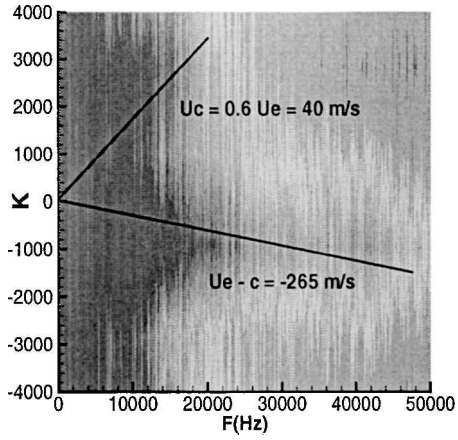

a) Leading edge

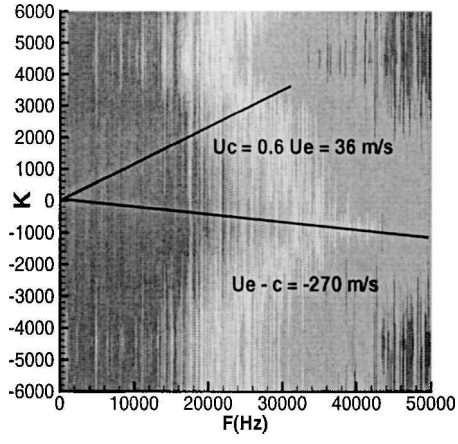

b) Bubble

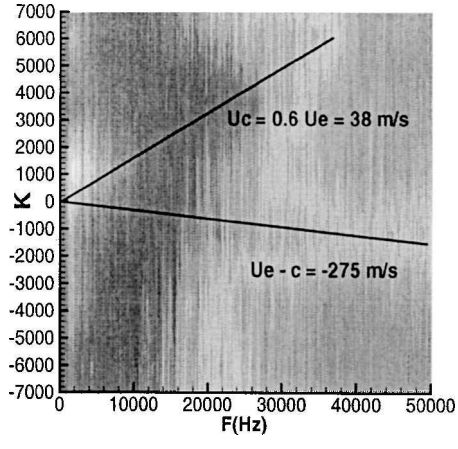

c) Trailing edge

Fig. 9 Wave-number-frequency spectra of wall-pressure fluctuations at different locations.

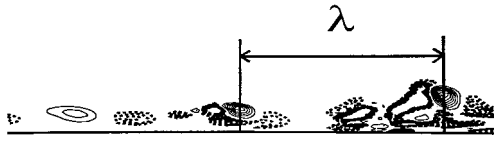

Fig. 10 Spatial Kelvin–Helmholtz length.

of the bubble, the profile has now two peaks, whereas at the third location ($x/C = 0.92$) three peaks are found. The same evolution was observed in wind-tunnel experiments by Lowson et al.,[27] who investigated the flow around a NACA airfoil at low Reynolds number. This evolution is related to the sudden amplification of upstream disturbances because of the existence of an inflexional velocity profile in the separated region of the flow, and it can be predicted using linear stability theory.[28]

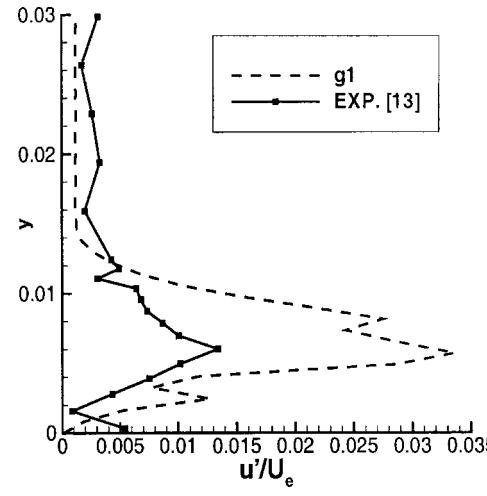

a)

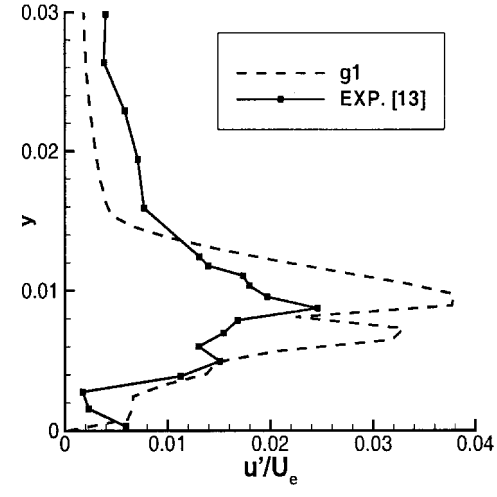

b)

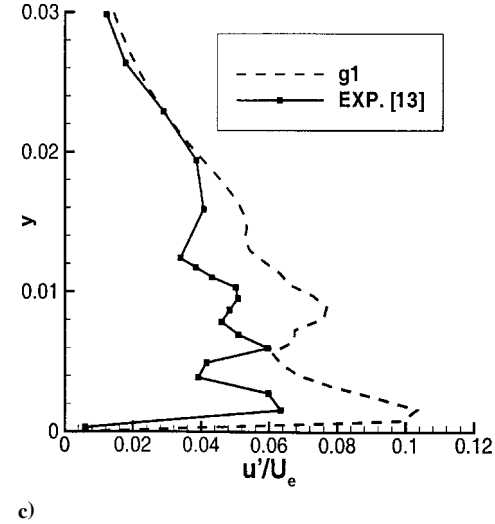

c)

Fig. 11 RMS velocity profiles around the transitional zone: a) x/C = 0.83, b) x/C = 0.88, and c) x/C = 0.92.

Global Dynamics of the Flow

As mentioned in the preceding section, a global feedback mechanism must exist to obtain sustained fluctuations inside the recirculation bubble. Another important feature of the flow is the vortex shedding that takes place at the trailing edge because that it is not sharp. The computed associated main frequency is 2500 Hz. Pressure spectra at the wall at three positions on the suction side are presented in Fig. 12. (For the sake of clarity, frequencies higher than 8000 Hz are not shown.) Inside the bubble (Fig. 12b) the peak

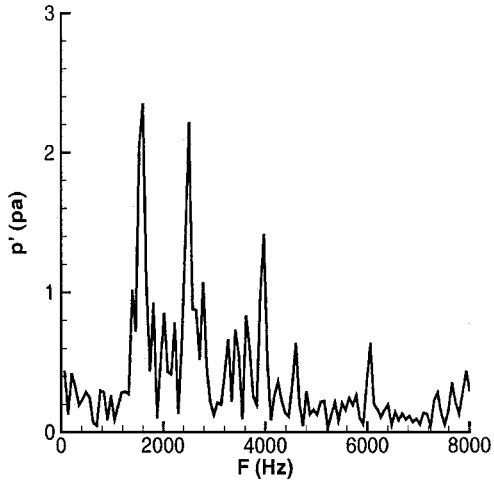

a) Leading edge

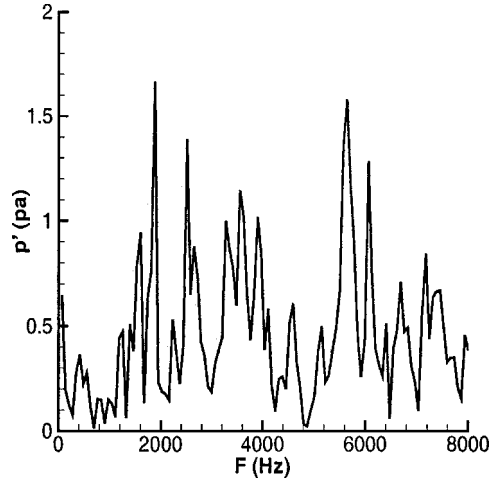

b) Bubble

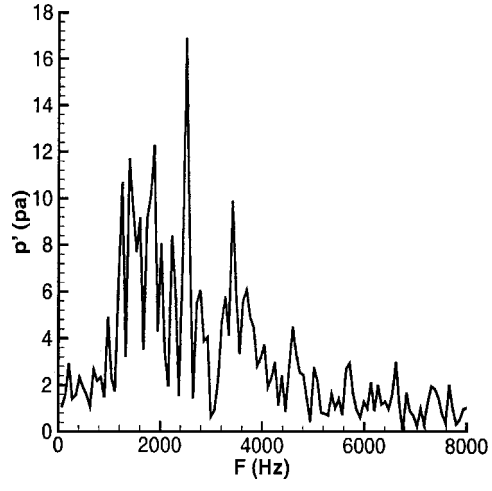

c) Trailing edge

Fig. 12 Frequency pressure spectra at different locations.

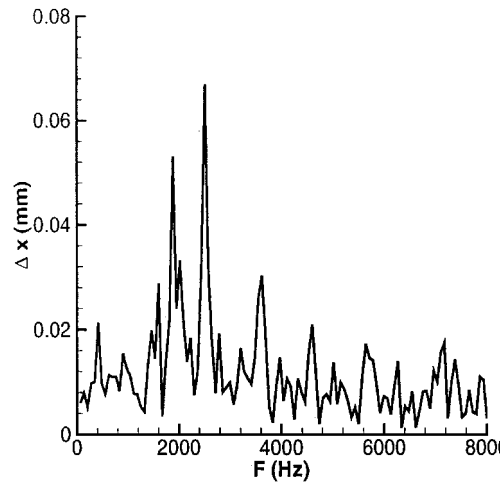

a)

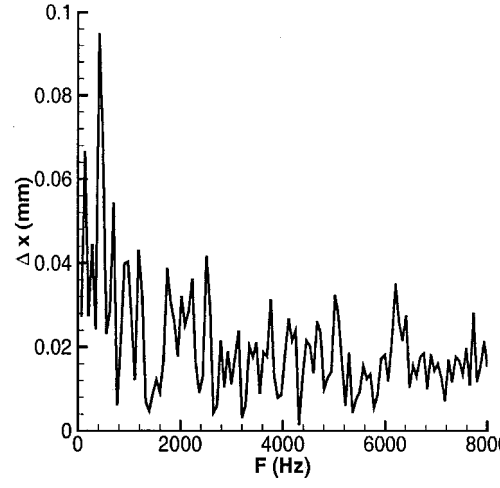

b)

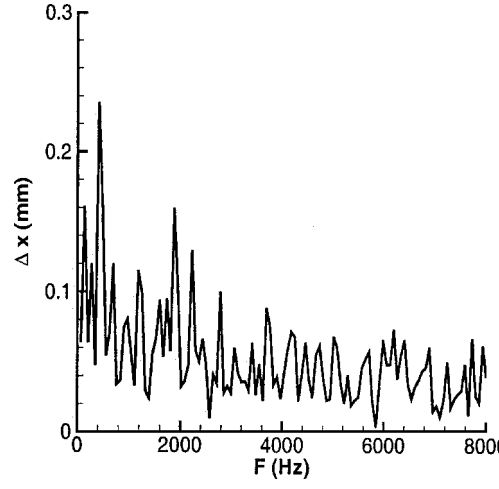

c)

Fig. 13 Frequency spectra of geometrical bubble characteritics at midspan: a) separation point x_s, b) reattachment point x_r, and c) length l_b.

related to the KH modes is clearly observed, as well as the peak associated with the vortex shedding frequency close to 2500 Hz. As noted by Yang and Voke,[10] the KH modes are associated with a range of frequencies around the most amplified one rather than single frequency. The large peak at 1900 Hz is related to the low-frequency flapping of the separated shear layer, which has been identified previously in many experiments and numerical simulations.[5,29–31] The corresponding Strouhal number based on U_e and $\langle l_b \rangle$ is 0.13, in good agreement with other observations.

Both separation $[x_s(t)]$ and reattachment $[x_r(t)]$ points exhibit a strongly unsteady behavior (see Fig. 6). Fast Fourier transform of these signals is presented in Fig. 13, together with the spectrum of the bubble length $[l_b(t)]$. The position of separation is clearly governed by the three mechanisms just cited: low-frequency flapping of the separated shear layer, KH instability, and vortex shedding at the trailing edge. At the contrary, the position of reattachment and the bubble length seem to be driven by another mechanism, associated with a lower frequency (500 Hz). A possible explanation for this phenomena is the existence of an aeroacoustic coupling between the vortex shedding at the trailing edge and the growth of

disturbances in the separated shear layer. Acoustic waves, which are observed to travel upstream, can excite the shear layer in the vicinity of the separation point, and the induced fluctuations then grow and travel downstream. Using the simple model proposed by Tam,[32] the corresponding frequency for the nth harmonics will be

$$f = n/(1/|U_e - c| + 1/U_c)L \tag{7}$$

where L is the distance between the separation point and the trailing edge. Taking $n = 1$, $U_c = 40\ \mathrm{m \cdot s^{-1}}$, $c - U_e = 270\ \mathrm{m \cdot s^{-1}}$, and $L = 0.0732$ m, the predicted value is 475 Hz, which is a satisfactory agreement. Taking $n = 4$ yields $f = 1900$ Hz, which is the value found for the low-frequency flapping, indicating a possible coupling between vortex shedding and the low-frequency flapping in the present case.

As already observed, upstream disturbances are necessary to maintain fluctuations inside the bubble. These disturbances can be seen on the left part of Fig. 10. To analyze their origin, the frequency/wave-number spectrum of the pressure fluctuations at the wall at the leading edge near the stagnation point and near the trailing edge is presented in Fig. 9. It is observed that acoustics waves traveling upstream are present everywhere but that no acoustic waves reflected at the stagnation point are detected. Vortical disturbances convected downstream at $U_c \approx 0.6U_e$ are also present all along the suction side. Then, a possible scenario is the following: acoustic waves are emitted near the trailing edge, which travel upstream up to the neighborhood of the stagnation point, where vortical disturbances are created and then convected downstream towards the recirculation bubble.

Conclusions

A new local mesh refinement technology has been successfully applied to a well-resolved large-eddy simulation of the flow around a low-pressure turbine blade at a realistic Reynolds number. The influence of the mesh resolution and the spanwise extent have been investigated. It appears that a grid convergence has been reached because the results are not influenced by these parameters. As the computed mean and fluctuating velocity profiles compare well with experimental data, the transition process has been studied in details. It occurs on the suction side of the blade thanks to a short laminar separation bubble. The shape of the bubble and the developement of Kelvin–Helmholtz instability in its shear layer are quite similar to those observed in Refs. 8–10 on a simpler geometry. However, a Fourier analysis applied to both the separation and reattachment points of the bubble underlines the existence of coupling between the bubble and the vortex shedding generated by the trailing edge.

Acknowledgments

This work was supported by the Consortium Industry Research Turbomachinery. P. Durbin is gratefully acknowledged for making available an early copy of the manuscript of Ref. 14. H. Hodson and L. Fottner very kindly provided the authors with experimental results.

References

[1]Gaster, M., "Structure and Behaviour of Laminar Separation Bubble," Aeronautical Research Council, R&M 3595, London, March 1967.

[2]Lisssaman, P. B. S., "Low-Reynolds-Number Airfoil," *Annual Review of Fluid Mechanics*, Vol. 15, 1983, pp. 223–239.

[3]Haase, W., Chaput, E., Elsholz, E., Leschziner, M., and Müler, U. (eds.), "ECARP—European Computational Aerodynamic Research Project: Validation of CFD Codes and Assessment of Turbulence Models," *Notes on Numerical Fluids Mechanics*, Vol. 58, Vieweg, Brunswick, Germany, 1997, pp. 325–346.

[4]Mary, I., and Sagaut, P., "Large-Eddy Simulation of Flow Around an Airfoil Near Stall," *AIAA Journal*, Vol. 40, No. 6, 2002, pp. 1139–1145.

[5]Pauley, L., Moin, P., and Reynolds, W., "The Structure of Two-Dimensional Separation," *Journal of Fluid Mechanics*, Vol. 220, 1990, pp. 397–411.

[6]Ripley, M., and Pauley, L., "The Unsteady Structure of Two-Dimensional Steady Laminar Separation," *Physics of Fluids A*, Vol. 5, No. 12, 1993, pp. 3099–3106.

[7]Wilson, P., and Pauley, L., "Two- and Three-Dimensional Large-Eddy Simulations of a Transitional Separation Bubble," *Physics of Fluids*, Vol. 10, No. 11, 1998, pp. 2932–2940.

[8]Alam, M., and Sandham, N. D., "Direct Numerical Simulation of Short Laminar Separation Bubbles with Turbulent Reattachment," *Journal of Fluid Mechanics*, Vol. 410, 2000, pp. 1–28.

[9]Spalart, P., and Strelets, M., "Mechanisms of Transition and Heat Transfer in a Separation Bubble," *Journal of Fluid Mechanics*, Vol. 403, 2000, pp. 329–349.

[10]Yang, Z., and Voke, P. R., "Large Eddy Simulation of Boundary Layer Separation and Transition at a Change of Surface Curvature," *Journal of Fluid Mechanics*, Vol. 439, 2001, pp. 305–333.

[11]Mayle, R. E., "The 1991 IGTI Scholar Lecture: The Role of Laminar-Turbulent Transition in Gas Turbine Engines," *Journal of Turbomachinery*, Vol. 113, No. 4, 1991, pp. 509–537.

[12]Engber, M., and Fottner, L., "The Effect of Incoming Wakes on Boundary Layer Transition of a Highly Loaded Turbine Cascade," AGARD, CP-571, May 1995.

[13]Hodson, H., "Turbulence Modelling for Unsteady Flows in Axial Turbine: TURMUNSFLAT," Brite-Euram Project, Final TR CT96-1043, von Kármán Inst., April 2000, pp. 85–99.

[14]Wu, X., and Durbin, P., "Evidence of Longitudinal Vortices Evolved from Distorted Wakes in a Turbine Passage," *Journal of Fluid Mechanics*, Vol. 446, 2001, pp. 199–228.

[15]Lenormand, E., Sagaut, P., and Ta Phuoc, L., "Large-Eddy Simulation of Subsonic and Supersonic Channel Flow at Moderate Reynolds Number," *International Journal for Numerical Methods in Fluids*, Vol. 32, No. 4, 2000, pp. 369–406.

[16]Boris, J. P., Grinstein, F. F., Oran, E. S., and Kolbe, R. L., "New Insights into Large Eddy Simulation," *Fluid Dynamic Research*, Vol. 10, 1992, pp. 199–228.

[17]Fureby, C., "Towards Large Eddy Simulation of Flows in Complex Geometries," AIAA Paper 98-2806, June 1998.

[18]Larchevêque, L., Labbé, O., Mary, I., and Sagaut, P., "LES of a Subsonic Flow over a Deep Open Cavity," *Proceedings of the Third AFOSR International Conference on DNS/LES*, Greyden Press, Columbus, OH, 2001, pp. 759–766.

[19]Mossi, M., "Simulation of Benchmark and Industrial Unsteady Compressible Turbulent Fluid Flows," Ph.D. Dissertation, No. 1958, Département Génie Mécanique, Ecole Polytechnique Fédérale de Lausanne, Lausanne, Switzerland, March 1999.

[20]Garnier, E., Mossi, M., Sagaut, P., Comte, P., and Deville, M., "On the Use of Shock Capturing Schemes for Large Eddy Simulation," *Journal of Computational Physics*, Vol. 153, No. 2, 1999, pp. 273–311.

[21]Péchier, M., Guillen, Ph., and Gayzac, R., "Magnus Effect over Finned Projectiles," *Journal of Spacecraft and Rockets*, Vol. 38, No. 4, 2001, pp. 542–549.

[22]Williamson, C. H. K., "Vortex Dynamics in the Cylinder Wake," *Annual Review of Fluid Mechanics*, Vol. 26, 1996, pp. 477–539.

[23]Quéméré, P., Sagaut, P., and Couaillier, V., "A New Multi-Domain/Multi-Resolution Method for Large Eddy Simulation," *International Journal for Numerical Methods in Fluids*, Vol. 36, No. 4, 2001, pp. 391–416.

[24]Raverdy, B., Mary, I., Sagaut, P., and Liamis, N., "LES of Flow Around a Low Pressure Blade Turbine," *Proceedings of Direct and Large Eddy Simulation Workshop 4*, edited by B. J. Geurts, R. Friedrich, and O. Metais, Kluwer Academic, Dordrecht, The Netherlands, 2001, pp. 201–204.

[25]Simpson, R. L., "A Review of Some Phenomena in Turbulent Flow Separation," *Journal in Fluids Engineering*, Vol. 103, 1981, pp. 520–533.

[26]Na, Y., and Moin, P., "Direct Numerical Simulation of a Separated Turbulent Boundary Layer," *Journal of Fluid Mechanics*, Vol. 374, 1998, pp. 379–405.

[27]Lowson, M., McAlpine, A., and Nash, E., "The Generation of Boundary Layer Instability Noise on Aerofoils," AIAA Paper 98-0627, Jan. 1998.

[28]Nash, E. C., and Lowson, M. V., "Noise due to Boundary Layer Instabilities," *Proceedings of the 1st CEAS/AIAA Joint Aeroacoustics Conference*, Vol. 2, Deutsche Gesellschaft fuer Luft- und Raumfahrt, Bonn, 1995, pp. 875–884.

[29]Dovgal, A. V., Kozlov, V. V., and Michalke, A., "Laminar Boundary Layer Separation: Instability and Associated Phenomena," *Progress in Aerospace Science*, Vol. 30, 1994, pp. 61–94.

[30]Niew, T. R., "The Stability of the Flow in a Laminar Separation Bubble," Ph.D. Dissertation, Univ. of Cambridge, Cambridge, England, U.K., 1993.

[31]Rist, U., Maucher, U., and Wagner, S., "Direct Numerical Simulation of Some Fundamental Problems Related to Transition in Laminar Separation Bubbles," *Proceedings of the Third ECCOMAS Computational Fluid Dynamics Conference*, edited by J. A. Désidéri, Wiley, New York, 1996, pp. 319–325.

[32]Tam, C. K. W., "Excitation of Instability Waves in a 2-D Shear Layer by Sound," *Journal of Fluid Mechanics*, Vol. 89, 1978, pp. 357–371.

P. Givi
Associate Editor